

# Molecular Mechanism and Microkinetic Analysis of the Reverse Water Gas Shift Reaction Heterogeneously Catalyzed by the Mo<sub>2</sub>C MXene

Anabel Jurado, Ángel Morales-García,\* Francesc Viñes, and Francesc Illas\*



Cite This: *ACS Catal.* 2022, 12, 15658–15667



Read Online

ACCESS |



Metrics & More



Article Recommendations

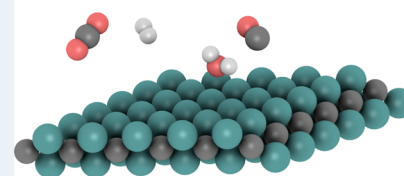


Supporting Information

**ABSTRACT:** The potential of the Mo<sub>2</sub>C MXene to catalyze the reverse water gas shift (RWGS) reaction has been investigated by a combination of density functional theory (DFT)-based calculations, atomistic thermodynamics, and microkinetic simulations. Different catalytic routes are explored including redox and associative (carboxyl and formate) mechanisms at a high temperature at which the RWGS reaction is exothermic. The present study predicts that, on the Mo<sub>2</sub>C MXene, the RWGS reaction proceeds preferentially through the redox and formate catalytic routes, the rate-limiting step being the formation of the OH intermediate followed by the H<sub>2</sub>O formation, whereas the carboxyl route to form the carboxyl intermediate is hindered by a large energy barrier. Microkinetic simulations confirm the formation of carbon monoxide (CO) under relatively mild conditions (i.e., ~400 °C and 1 bar). The CO formation is not affected either by the total pressure or by the CO<sub>2</sub>/H<sub>2</sub> ratio. However, water formation requires high temperatures of ~700 °C and pressures above 5 bar. In addition, an excess of hydrogen in the CO<sub>2</sub>/H<sub>2</sub> ratio favors water formation. Shortly, the present study confirms that the Mo<sub>2</sub>C MXene emerges as a heterogeneous catalyst candidate for generating a CO feedstock that can be used for subsequent transformation into methanol through the Fischer–Tropsch process.

**KEYWORDS:** Mo<sub>2</sub>C, MXene, reverse water gas shift, density functional theory, microkinetics

## MXenes for RWGS



## 1. INTRODUCTION

Catalysis has generated a great impact in the human societies being at the forefront of addressing fundamental challenges in climate change, sustainable energy, and food supply.<sup>1</sup> To date, more than 80% of all chemical products in the world are produced via heterogeneous catalysis. Henceforth, the design and development of new robust and selective catalysts continue being imperative to maintain the present welfare state.<sup>2</sup> In this context, new catalysts with high affinity for carbon dioxide (CO<sub>2</sub>) are demanded with the goal of development technologies for capturing and utilizing CO<sub>2</sub>.<sup>3,4</sup>

In principle, high-volume chemicals can be produced from CO<sub>2</sub> through carbon capture and utilization (CCU) strategies by using a specific heterogeneous catalyst: the dry reforming of methane (DRM) or ethanol (DRE), methanol synthesis, the CO<sub>2</sub> methanation (known as Sabatier reaction), and the reverse water gas shift (RWGS) reactions are some examples of heterogeneous catalytic reactions where the CO<sub>2</sub> is transformed into chemicals or hydrocarbon fuels. Especially interesting is the RWGS reaction: CO<sub>2</sub> + H<sub>2</sub> → CO + H<sub>2</sub>O. This is a fundamental step providing a CO feedstock for methanol synthesis through the efficient Cu/ZnO catalysts with possible subsequent transformation to acetic acid through the Monsanto/Cativa process or to hydrocarbon through the Fischer–Tropsch synthesis. Due to the large impact of the RWGS reaction in heterogeneous catalysis, several catalysts have been investigated and developed. Initially, reduced

inorganic oxides such as CeO<sub>2</sub>, ZnO, Al<sub>2</sub>O<sub>3</sub>, Fe<sub>2</sub>O<sub>3</sub>, or MnO<sub>2</sub> were used.<sup>5–7</sup> However, such oxides present drawbacks as low CO<sub>2</sub> activation and easy sintering. To overcome these limitations, composite oxides, spinel oxides, solid solution oxides, and perovskite-type oxides have been investigated showing a structural stability and reverse oxygen storage to increase RWGS performance.<sup>8–11</sup> In addition, supported metal catalysts involving for instance Pt, Pd, or Au anchored onto the metal oxide support material facilitate the CO<sub>2</sub> activation in the metal/oxide interfaces making suitable catalysts for the RWGS reaction,<sup>12,13</sup> although there is clear room for improvement.

In this quest for heterogeneous catalysts for the RWGS, transition metal carbides (TMCs) emerged as a possible alternative due to their similar properties to precious metal-based catalysts.<sup>14</sup> The incorporation of carbon in the metal lattice induces new chemistry from the metallic counterparts affecting to the binding energy and the reactivity of adsorbates.<sup>15</sup> Particularly, Mo<sub>2</sub>C is interesting for CO<sub>2</sub>

**Received:** September 12, 2022

**Revised:** November 22, 2022

conversion because of its good performance for  $\text{H}_2$  dissociation and CO bond scission, two key chemical aspects required in the RWGS reaction.<sup>16–18</sup> During this process, the dissociation of  $\text{CO}_2$  into  $\text{CO} + \text{O}$ , the formation of oxycarbide species, and the facile removal of oxygen from the  $\text{Mo}_2\text{C}$  surface by  $\text{H}_2$  were found to be the key steps for achieving high activity, selectivity, and stability of  $\text{Mo}_2\text{C}$ .

Recently, low-dimensional carbides known as MXenes have been successfully synthesized.<sup>19,20</sup> MXenes are produced through a top-down synthesis procedure from layered ternary materials known MAX phases with the chemical formula  $\text{M}_{n+1}\text{AX}_n$  ( $n = 1–3$ ), where M is an early transition metal, A represents XIII- and XIV-group elements, and X stands for C and/or N atoms. The M–A chemical bond is susceptible to chemical etchant agents promoting the disassembly of the MAX phase and forming the  $\text{M}_{n+1}\text{X}_n\text{T}_x$  or MXene phases. Normally, the as-synthesized MXene phases are functionalized depending on the etchant employed in the chemical exfoliation. Such functionalization is represented by the  $\text{T}_x$  term, where  $x$  indicates a non-stoichiometric termination. HF, LiF/HCl, or  $\text{NH}_4\text{HF}_2$  are the most regular etchants employed to break the M–A bond.<sup>21</sup> Although this top-down procedure drives to functionalized MXenes, recent work reported a strategy combining high-temperature and hydrogenation reaction to generate defunctionalized (clean or bare) MXenes.<sup>22</sup> In addition, new synthetic routes using alkali halides as etchant agents lead to produce MXene with not so strong bonded halide ( $\text{T}_x = \text{Cl}$  or  $\text{Br}$ ) that further facilitates the generation of bare MXenes.<sup>23</sup>

Bare MXenes have been predicted to exhibit an outstanding performance in the activation of the  $\text{CO}_2$  molecule, later confirmed by experiments.<sup>22,24,25</sup> These results demonstrate the feasibility of these MXene materials for carbon capture and storage (CCS) procedures. However, clean MXenes result even more interesting because they can dissociate  $\text{CO}_2$  into  $\text{CO} + \text{O}$  requiring energy barriers below 0.6 eV that makes them also appropriate candidates for CCU.<sup>26</sup> Furthermore, MXenes easily dissociate  $\text{H}_2$  with almost negligible barriers.<sup>27</sup> Thus, MXenes meet the main conditions of suitable substrates for the RWGS reaction. In addition, MXenes preserve the physical and chemical properties of their 3D carbide counterparts together with a large surface area, as described recently in detail by some of us.<sup>28</sup> Furthermore, experimental analysis has confirmed the stability of  $\text{Ti}_3\text{C}_2$  MXene up to 800 °C.<sup>29</sup>

To assess the suitability of MXene as candidate heterogeneous catalysts for the RWGS reaction, we present a multiscale analysis on the bare  $\text{Mo}_2\text{C}$  MXene phase with an ABC stacking.<sup>30</sup> This choice is based on a prescreening step evidencing that this particular MXene exhibits moderate binding energies of reactant and intermediates that make feasible the progression of the reaction. Furthermore, its choice is based on the good performance of its bulk  $\text{Mo}_2\text{C}$  counterpart.<sup>31</sup> The present study combines first-principles calculations and microkinetic simulations to investigate in detail the mechanisms of the RWGS reaction via redox and associative routes, see Figure 1.<sup>7</sup> Noting that associative routes involve the formation of carbon-containing intermediates, namely, formate and carboxyl.

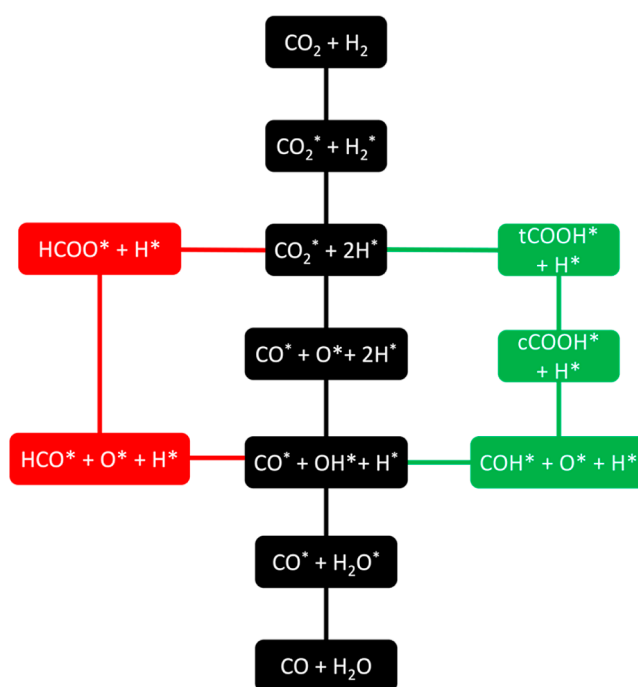


**Figure 1.** Scheme of the investigated RWGS reaction sequences including redox (black), associative carboxyl, that is, COOH (green), and associative formate, that is, HCOO (red).

## 2. COMPUTATIONAL DETAILS AND MATERIALS MODELS

The present study combines periodic density functional theory (DFT)-based calculations and microkinetic simulations. The DFT calculations are carried out by means of the Vienna Ab Initio Simulation Package (VASP)<sup>32</sup> with exchange and correlation effects accounted through a generalized gradient approximation (GGA) as described by the Perdew–Burke–Ernzerhof (PBE) density functional.<sup>33</sup> Furthermore, the dispersion interactions were included through Grimme’s D3 approach.<sup>34</sup> A cutoff energy of 415 eV were selected to expand the valence electron density using a plane-wave basis set, whereas the effect of the core electrons on the valence density was described using the projector augmented wave (PAW) method.<sup>35</sup> For the unit cell described below, the numerical integration in the reciprocal space was carried out using a  $\Gamma$ -centered  $5 \times 5 \times 1$   $k$ -point grid in the Brillouin zone. The convergence threshold for the geometry optimization calculations is reached when the forces on all atoms are below 0.01 eV·Å<sup>−1</sup> and the relaxation of the electronic degrees of freedom steps is 10<sup>−6</sup> eV. Note that this computational scheme has been used in previous works, reporting results with accuracy below 0.04 eV.<sup>24–29</sup>

The RWGS reaction is studied using a  $p(3 \times 3)$  supercell representing the basal (0001) plane of  $\text{Mo}_2\text{C}$  with an ABC stacking of the atomic layers, see Figure 2. Larger supercells give similar results to the  $p(3 \times 3)$  supercell used in the present work. Looking at the top side of the MXene surface, one may identify easily four high-symmetry sites including on-top of a surface Mo site (T), bridging two vicinal surface Mo sites (B), and two threefold hollow sites involving three surface Mo atoms, having one Mo atom two layers underneath ( $\text{H}_M$ ), or one C atom a layer underneath ( $\text{H}_C$ ). The slabs are separated by a vacuum of at least 10 Å in the [0001] direction to vanish the interaction between the periodic replicas as the model used

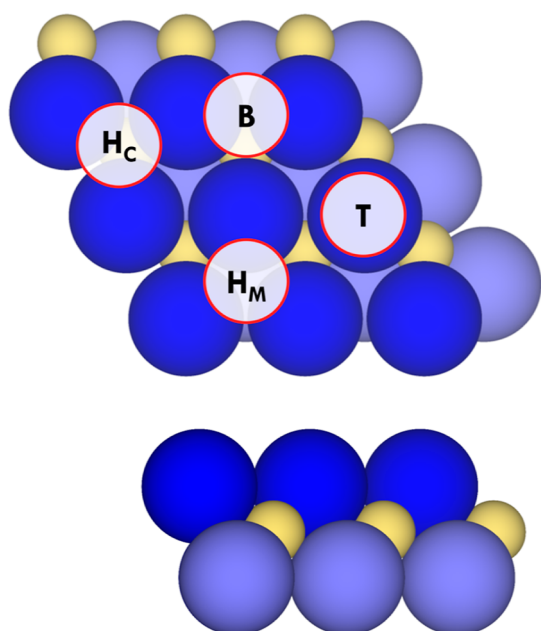


**Figure 2.** Top (top) and side (bottom) views of the Mo<sub>2</sub>C (0001) surface  $p(3 \times 3)$  supercell. C atoms are represented by yellow spheres, while Mo atoms are represented by dark and light blue spheres to distinguish upmost and bottommost layers. The four relevant high-symmetry sites are depicted as T, B, H<sub>M</sub>, and H<sub>C</sub> labels identifying top, bridge, hollow metal, and hollow carbon sites, respectively.

is periodic in the three dimensions of space. The adsorption energy,  $E_{\text{ads}}$ , of the reactants and products, denoted by the term of species, is calculated as

$$E_{\text{ads}} = E_{\text{species}@Mo_2C} - (E_{\text{species}} + E_{Mo_2C}) + \Delta ZPE \quad (1)$$

where  $E_{\text{species}@Mo_2C}$  is the total energy of the corresponding species adsorbed, that is, reactants or products, on the Mo<sub>2</sub>C

MXene,  $E_{\text{species}}$  stands for their energy in gas phase, while  $E_{Mo_2C}$  corresponds to the energy of the pristine MXene slab model. The  $E_{\text{species}}$  is calculated isolating the species in an asymmetric box with  $10 \times 11 \times 12 \text{ \AA}$  dimensions and considering the  $\Gamma$ -point only. The term  $\Delta ZPE$  stands for the difference in the zero-point energy contribution between the adsorbed and phase gas species. This term is obtained directly from the vibrational frequencies in gas phase and those vibrational modes once the species is anchored to the surface. The latter includes the vibrational modes coming from the frustrated translational and rotational degrees of freedom; see Table S1 in the Supporting Information. The frequencies are obtained by diagonalization of the corresponding block of the Hessian matrix with elements computed as finite differences of analytical gradients with displacements of  $0.03 \text{ \AA}$ . In all cases, calculations were sufficiently refined to ensure that all adsorbed species exhibit real frequencies and transition states only one imaginary frequency corresponding to the reaction coordinate.

The search for the transition states (TSs) of each step listed in Table 1 was carried out using climbing-image nudged elastic band (CI-NEB) and dimer methods, the former including five intermediate images and minimizing forces acting on atoms below  $0.03 \text{ eV}\cdot\text{\AA}^{-1}$ .<sup>36,37</sup> Frequency analyses was carried out over the located TS structures to ensure that just one imaginary frequency was identified along the reaction pathway. In each step, the initial atomic configurations used to locate TSs were the most stable adsorption configuration. The activation energy barrier,  $E_a$ , is thus calculated as the difference between the TS and the initial configuration, and its energy includes the ZPE contribution. All these minima and reaction step energy barriers allow one outlining the free-energy profile along the coordination reaction at certain temperature and gas pressure using the Ab initio thermodynamics (AIAT) framework.<sup>38</sup>

The identification of reaction intermediates and rate-limiting elementary reaction of the RWGS reaction is carried out using

**Table 1. Elementary Reaction Steps of the RWGS Reaction<sup>a</sup>**

step	elementary reaction step	forward			backward	
		$E_{a,i}$	$A_i$	$\Delta E$	$E_{a,i}$	$A_i$
1	CO <sub>2</sub> (g) → CO <sub>2</sub> *					
2	H <sub>2</sub> (g) → H <sub>2</sub> *					
3	CO* → CO(g)					
4	H <sub>2</sub> O* → H <sub>2</sub> O(g)					
5	H <sub>2</sub> * → 2H*	0.01	$8.35 \times 10^{12}$	-0.81	0.93	$8.88 \times 10^{13}$
6	CO <sub>2</sub> * → CO* + O*	0.47	$4.31 \times 10^{13}$	-1.43	1.90	$8.86 \times 10^{12}$
7	O* + H* → OH*	1.59	$1.99 \times 10^{13}$	0.88	0.70	$1.67 \times 10^{13}$
8	OH* + H* → H <sub>2</sub> O*	1.68	$3.04 \times 10^{14}$	1.36	0.32	$1.15 \times 10^{13}$
9	CO <sub>2</sub> * + H* → HCOO*	0.56	$2.34 \times 10^{14}$	0.08	0.48	$7.49 \times 10^{13}$
10	HCOO* → HCO* + O*	0.29	$3.03 \times 10^{13}$	-1.00	1.30	$4.53 \times 10^{13}$
11	HCO* → H* + CO*	0.36	$1.67 \times 10^{13}$	-0.50	0.86	$1.99 \times 10^{13}$
12	CO <sub>2</sub> * + H* → tCOOH*	0.84	$7.93 \times 10^{13}$	0.83	0.01	$4.40 \times 10^{13}$
13	tCOOH* → cCOOH*	0.27	$2.08 \times 10^{13}$	-0.07	0.34	$2.53 \times 10^{13}$
14	cCOOH* → COH* + O*	0.49	$1.32 \times 10^{13}$	-0.81	1.30	$2.00 \times 10^{12}$
15	COH* → CO* + H*	0.62	$1.50 \times 10^{13}$	-1.40	1.43	$2.03 \times 10^{13}$

<sup>a</sup>The relevant kinetic parameters of the RWGS reaction over the Mo<sub>2</sub>C MXene surface are the activation barriers,  $E_a$ , given in eV, and pre-exponential factors,  $A_i$ , given in  $\text{s}^{-1}$ , both shown for forward and backward reactions. Reaction energies,  $\Delta E$ , given in eV, are listed for each elementary reaction in the forward reaction, but note that  $\Delta E_{\text{forward}} = -\Delta E_{\text{backward}}$ . The activation energy values include the ZPE contribution, whereas  $A_i$  factors are obtained from the intercept of the of the Arrhenius linear plot when representing the  $\text{Ln}(\text{rate})$  of each elementary reaction step versus  $1/T$ . This is the limit of  $A_i$  for  $T \rightarrow \infty$ . The steps corresponding to adsorption/desorption of reactants (CO<sub>2</sub> and H<sub>2</sub>) and products (CO and H<sub>2</sub>O) are included just for consistency with the labeling of steps in the microkinetic study.

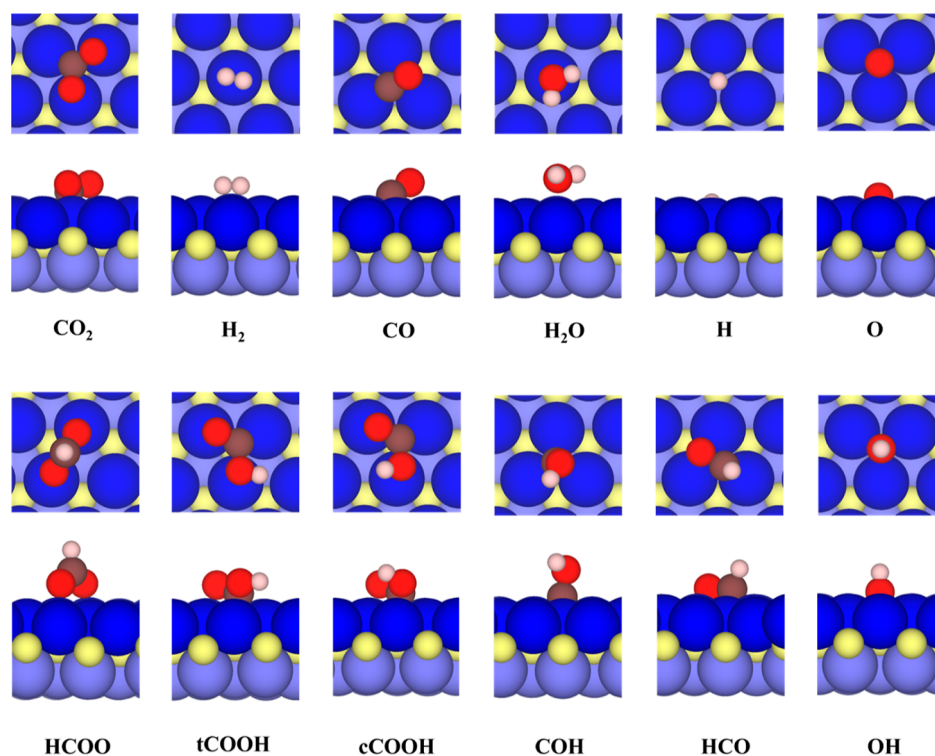


**Figure 3.** Most stable adsorption sites for CO<sub>2</sub>, H<sub>2</sub>, CO, H<sub>2</sub>O, H, O, HCOO, tCOOH, cCOOH, COH, HCO, and OH on the Mo<sub>2</sub>C MXene (0001) surface. Color coding for MXene as in Figure 1, whereas brown, red, and white spheres denote C, O, and H atoms, respectively.

microkinetic modeling as implemented in the MKMCXX program.<sup>39</sup> Our microkinetic model is based on 15 elementary steps for studying the RWGS reaction; see Table 1. The redox mechanism and the associative mechanisms via formate (HCOO) or carboxyl (COOH) intermediates are analyzed. In short, the redox route follows the 1 → 2 → 5 → 6 → 7 → 8 → 3 → 4 sequence, see Table 1; whereas formate route and carboxyl routes imply the 1 → 2 → 9 → 10 → 11 → 7 → 8 → 3 → 4 and 1 → 2 → 12 → 13 → 14 → 15 → 7 → 8 → 3 → 4 sequences, respectively. Note that CO<sub>2</sub> and H<sub>2</sub> adsorptions—steps 1 and 2, respectively—, OH\* and H<sub>2</sub>O\* formations—steps 7 and 8, respectively—, and the CO and H<sub>2</sub>O desorptions—steps 3 and 4, respectively—are common for the three mechanisms.

The parameters defining the rates of the surface and desorption reaction steps were estimated from transition state theory (TST),<sup>40,41</sup> including activation energy barriers and the partition functions accounting for the vibration degrees of freedom of ground state and TSs. For surface reactions, constants were estimated through the equation.

$$k = \frac{k_B T}{h} \frac{Q^{\text{TS}}}{Q} e^{-E_a/k_B T} \quad (2)$$

where  $Q$  and  $Q^{\text{TS}}$  correspond to the partition functions of the initial state and TS, respectively. The reaction rate constant for unimolecular adsorption is calculated using the collision theory as

$$k_{\text{ads}}^i = \frac{A_{\text{site}} \cdot p_i \cdot S_i}{\sqrt{2 \cdot \pi \cdot m_i \cdot k_B \cdot T}} \quad (3)$$

where  $A_{\text{site}}$  is the area of the adsorption site and is calculated by dividing the supercell area of the (0001) surface by the total number of sites in it;  $p_i$  stands for the partial pressure of the

component  $i$ ;  $S_i$  corresponds to the sticking coefficient of the component  $i$ ; and  $m_i$ ,  $k_B$ , and  $T$  are the molecular mass, Boltzmann's constant, and working temperature, respectively. Last but not least, note that the sticking coefficient of reactants and products was fixed to 1.0. This selection was based on previous estimations of this coefficient for these molecules on Pt surfaces, where the interaction of the molecules was of the same order of magnitude reporting high  $S_i$  values above 0.7,<sup>43–45</sup> and, therefore, no significant influence is expected from this variable in the optimal conditions at which the RWGS reaction proceeds which is confirmed by additional simulations varying this parameter. Further details are given in Table S2 in the Supporting Information.

The steady-state surface coverage for each adsorbed species,  $\theta_i$ , were calculated by solving the differential equations over time of each intermediate  $i$ , where the steady-state solution is reached when  $\frac{\partial \theta_i}{\partial t} = 0$ .<sup>39</sup> These coverage values were next used to calculate the rates of the individual elementary reaction steps and the overall rate per surface atom. Lateral interactions and their influence on activation barriers were not considered in this study. The present microkinetic simulation rely on a mean-field approximation in which interactions between the adsorbed species are neglected, and all species are randomly distributed over the Mo<sub>2</sub>C MXene surface. The kinetic database used as input for the microkinetic simulations is reported in Table 1, with additional details given in the Supporting Information. Our simulations only include the initial partial pressure of reactants (i.e., CO<sub>2</sub> and H<sub>2</sub>), which is consistent with the design of a given type of differential reactor in which products are constantly removed. This reactor consists of a thin catalyst bed, which results in a small conversion of reactants into products. In other words, the zero-conversion approximation is considered because the focus is on

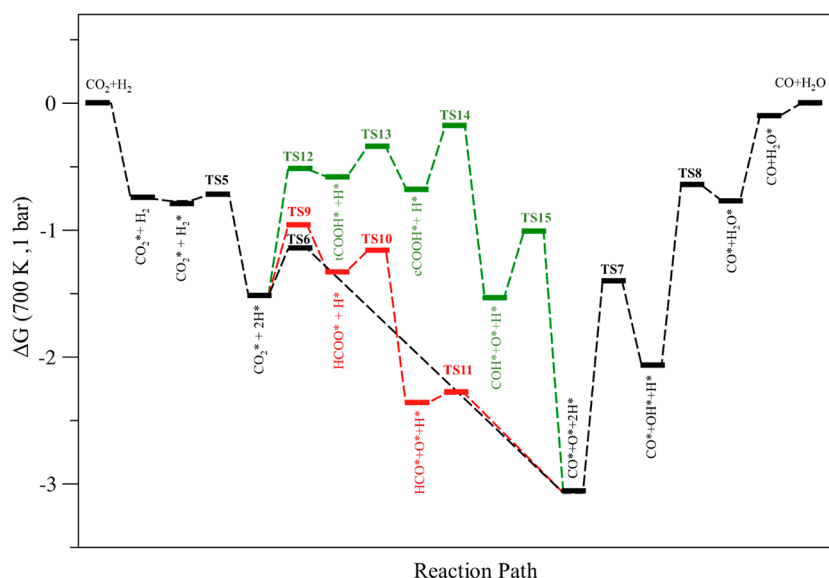


**Figure 4.** Calculated Gibbs free energy,  $\Delta G$ , given in eV, profile of the redox (black), HCOO (red), and COOH (green) route mechanisms for the RWGS reaction on the  $\text{Mo}_2\text{C}$  MXene (0001) surface. The TSs are identified in consistency with the reaction elementary step number as listed in Table 1.

the behavior of  $\text{Mo}_2\text{C}$  MXene as a suitable catalyst for the RWGS reaction.

### 3. RESULTS AND DISCUSSION

**3.1. Total Energy and Gibbs Free Energy Profiles.** We start by exploring the adsorption energy landscape for the different gas phase species involved in the RWGS reaction on the basal (0001) plane of the  $\text{Mo}_2\text{C}$  MXene model, depicted in Figure 2. This analysis involves the  $\text{CO}_2$  and  $\text{H}_2$  reactants and  $\text{CO}$  and  $\text{H}_2\text{O}$  products in their most stable configuration, as shown in Figure 3. The calculated  $E_{\text{ads}}$  values for reactants and products are  $-1.80$ ,  $-0.79$ ,  $-2.39$ , and  $-0.95$  eV including ZPE correction for the  $\text{CO}_2$ ,  $\text{H}_2$ ,  $\text{CO}$ , and  $\text{H}_2\text{O}$  molecules, respectively. These exothermic adsorption energies agree with those in previous work published by some of us.<sup>27,29</sup> Among them, the largest activation corresponds to  $\text{CO}$  followed by  $\text{CO}_2$ , whereas the  $E_{\text{ads}}$  values for  $\text{H}_2$  and  $\text{H}_2\text{O}$  are below  $-1$  eV, indicating that, in these cases, the molecular interaction can well correspond to a physisorption process. Similar  $\text{H}_2$  molecular interaction, known as the Kubas state, has been observed in other supports such as graphene.<sup>46</sup> The interactions of  $\text{CO}_2$ ,  $\text{H}_2$ , and  $\text{H}_2\text{O}$  with the  $\text{Mo}_2\text{C}$  (0001) surface are in a parallel orientation to the MXene surface; meanwhile, the  $\text{CO}$  molecule interacts through its C atom with a certain tilt locating the O atom far from the surface, see Figure 3.

The reaction energy,  $\Delta E$ , of the RWGS reaction in gas phase calculated with the PBE exchange–correlation functional is 0.85 eV which deviates significantly from the experimental reaction enthalpy of 0.42 eV ( $40.52 \text{ kJ mol}^{-1}$ ) at room temperature.<sup>47</sup> On the other hand, accurate predictions based on coupled cluster singles and doubles (CCSD) report  $\Delta E$  equal to 0.39 eV, thus close to the experimental value. We note that CCSD results are introduced just to compare with our PBE results. Clearly, the difference between PBE and CCSD or experiments is due to intrinsic errors of these DFT-based methods, an error that can be minimized by correcting the DFT-based gas phase values accounting for DFT systematic errors on the energy of gas phase molecules.<sup>48</sup> Because the

error in the energy of  $\text{H}_2$  and  $\text{H}_2\text{O}$  is negligible, we extract the  $\text{CO}_2$  and  $\text{CO}$  PBE energy corrections from the values provided for the errors in the standard Gibbs formation energy reported in ref 48. These were computed using experimental entropy values, the error in the Gibbs formation energy arises solely from the DFT energy. Thus, we used values of  $-0.19$  and  $0.24$  eV for  $\text{CO}_2$  and  $\text{CO}$ , respectively. Taking into account these errors, the calculated  $\Delta E$  becomes 0.42 eV, matching the experiment. Shortly, the RWGS reaction is an endothermic process and thus requires high temperature to shift the equilibrium toward product formation. This is confirmed by calculating the reaction Gibbs free energy,  $\Delta G$ , at a temperature of 700 K and partial gases pressures of 1 bar, which, including the total energy correction for gas phase errors, becomes  $-0.09$  eV at 700 K, see Figure 4, and even more exergonic at 1000 K, with  $\Delta G = -0.29$  eV.

The total errors in the formation energy of  $\text{CO}_2$  and  $\text{CO}$  represent the difference between DFT Gibbs formation energy and the experimental value. These errors in the standard free energies are density functional-dependent so that the signs and magnitude change in each case. In this work, we apply a semiempirical correction to estimate the corresponding values at room temperatures as the standard total entropies and the experimental standard free energies were obtained from thermodynamic tables at such temperatures. Further details about this semiempirical correction can be found in ref 48.

Once the energy minima of the involved species shown in Figure 3 are identified and properly characterized, we proceeded to investigate the energy barriers required to be surmounted in each one of the elementary reaction steps; see Figure S2 in the Supporting Information to visualize the TSs. The kinetic parameters of each elementary step are listed in Table 1, and the Gibbs energy profile at 700 K and 1 bar of gases partial pressures is depicted in Figure 4 showing that the RWGS reaction progresses through either the redox or the associative mechanisms. The former requires explicitly the dissociation of  $\text{CO}_2^*$  into  $\text{CO}^* + \text{O}^*$ , whereas the latter ones involve alternative pathways where the  $\text{CO}_2^*$  molecule is hydrogenated and the reaction thus advances through different

carbon-containing intermediates. For completeness, the calculated energy profile is shown in Figure S1 in the Supporting Information.

Focusing on the redox (black) route, see Figures 1 and 4, the RWGS reaction starts by the H<sub>2</sub> dissociation to form two H\* adatoms followed by the dissociation of CO<sub>2</sub> into CO\* and O\* adsorbed species. Here, breaking the CO<sub>2</sub> molecule demands an energy barrier of 0.47 eV only. The rest of the route involves the formation of water from the O\* and H\* adatoms. However, the formation of OH\* requires a high energy barrier of 1.59 eV to be overcome, and even the subsequent formation of H<sub>2</sub>O is uphill with a demand of 1.68 eV of energy. Therefore, these two latter reaction steps constitute the rate-determining steps in the redox route. Interestingly, a similar rate-determining step was found on the Cu@Mo<sub>2</sub>C(001) catalyst involving the corresponding bulk carbide, where the step for OH\* formation had an activation barrier of 1.14 eV.<sup>49</sup>

A second competitive pathway involves HCOO\* formation (red), see Figures 1 and 4. This is formed by the CO<sub>2</sub>\* hydrogenation requiring surmounting a mild barrier of 0.56 eV. From here on, the following steps involve the sequential dissociation reaction to produce CO\*. The first one corresponds to the formation of HCO\*, followed by its dissociation into CO\* + H\*. The two sequential dissociation steps demand quite low activation energies of 0.29 and 0.36 eV, respectively. The interaction of HCO\* intermediate with the Mo<sub>2</sub>C (0001) MXene surface implies that the C=O fragment lays planar and in full contact with the surface of catalyst, see Figure 2, which may justify the low activation energy required to obtain CO\*. Finally, similar to the redox route, the steps for the formation of OH\* and H<sub>2</sub>O\* species constitute the rate-limiting steps. We notice that the formation of HCOOH, a plausible product, requires a large energy barrier (2.21 eV) compared to that leading to the HCOO\* intermediate dissociation to HCO\* + O\*, making thus the formation of formaldehyde a kinetically inhibited process.

The third pathway (green) proceeds through the formation of the COOH carboxyl intermediate, see Figure 4, produced by activating and hydrogenating the CO<sub>2</sub> molecule leading to COOH\*.<sup>50</sup> In particular, the *trans*-COOH (tCOOH\*) species is formed with an activation barrier of 0.84 eV. Later, there is a conformational transition toward *cis*-COOH (cCOOH\*), with an activation barrier of solely 0.27 eV. This later intermediate is then first dissociated into COH\* plus O\* and later into CO\* plus H\* featuring energy barriers of 1.30 and 0.62 eV, respectively. The present calculations confirm that the tCOOH\* formation, with an E<sub>a</sub> of 0.84 eV, is not fully competitive compared to the redox or the formate formation, with values of 0.47 and 0.56 eV, respectively, so probably the path is not really followed, or at a negligible pace compared to the other two mechanisms, even though the carboxyl mechanism was previously confirmed to be followed, and cCOOH\* dissociation being a rate-determining step in the RWGS reaction involving Ni<sub>n</sub>/YSZ(111) interfaces.<sup>51</sup>

Thus, from the free energy profile depicted in Figure 4, one concludes that the Mo<sub>2</sub>C MXene constitutes an optimal candidate for the heterogeneously catalyzed RWGS reaction, as this reaction takes place with affordable energy barriers, yet the rate-determining steps of the RWGS reaction involve the formation of OH\* and H<sub>2</sub>O\* regardless the followed mechanistic route, together with the CO and H<sub>2</sub>O products desorption. This implies that the reaction requires high a working temperature and gas pressures to be carried out, a

point nevertheless dictated by the reaction thermodynamics, because, obviously, the catalyst effect is actually on the kinetics only. To further clarify this latter issue, microkinetic simulations are carried out to identify the optimal conditions to generate CO and H<sub>2</sub>O.

**3.2. Microkinetic Analysis.** We now focus on microkinetic simulations to predict surface coverages and relative product selectivity including the detection of most abundant reaction intermediates. Based on the DFT data from Table 1, we developed different microkinetic models to further investigate the activity of the Mo<sub>2</sub>C MXene catalyst under different T/p<sub>i</sub> working conditions. To select the working conditions of the simulations, we relied on literature for Molybdenum carbide-derived catalysts that have shown good performance for the RWGS reaction. Thus, 1% Cu@β-Mo<sub>2</sub>C and 7.5% Co@Mo<sub>2</sub>C have shown selectivities of 40 and ~98.1% for the RWGS using 2:1 H<sub>2</sub>/CO<sub>2</sub> ratio at 300 °C and 0.1 and 1.07 × 10<sup>-4</sup> MPa (10 and 1.07 × 10<sup>-3</sup> bar), respectively.<sup>16,52</sup> Bare Mo<sub>2</sub>C catalysts have shown as well an outstanding selectivity above 90% under the same conditions of 7.5% Co@Mo<sub>2</sub>C.<sup>16</sup> These available experimental data are taken as the reference for setting the working conditions to perform microkinetic simulations of the RWGS reaction over Mo<sub>2</sub>C MXene.

Thus, the microkinetic simulations have been carried at three different total pressures (i.e., 1, 5, and 10 bar) and using a H<sub>2</sub>/CO<sub>2</sub> ratio of 2:1. The evolution of the coverage of the different adsorbed species with the temperature is shown in Figure 5. The total pressure has an influence on the coverage in the temperature window of 300–550 K. Here, one observes that the HCOO\* species has a coverage slightly above 0.1 at 1 bar, and increases reaching coverages of 0.3 and 0.4 at 5 and 10 bar, respectively. The HCO\* coverage is around 0.4 regardless the total pressure. On the other hand, the CO\* species is also present at the MXene catalyst surface regardless the total pressure because CO desorption starts at 700 K. Finally, the presence of O\* starts to be important at 400 K and above such temperature increases exponentially promoting the O-functionalization of the Mo<sub>2</sub>C MXene surface, a trend that is systematically observed regardless the total pressure as well. For practical applications, the catalysts surface may need to be regenerated after a few cycles. Note that the steady-state is reached at short timescales when the production/consumption rate of the gas species is constant. However, from a microkinetic viewpoint, and because the MXene trends to functionalize its surface, it is more reasonable to describe this process as a “quasi-steady state”.

The present microkinetic simulations reveal that the RWGS reaction progresses through the formate associative mechanism beyond 200 K, where the formation of HCOO\*, with an E<sub>a</sub> of 0.56 eV is overcome. From 300 K on, the HCO\* formation is observed, overcoming the E<sub>a</sub> of 0.29 eV. Above 350 K, the formation of the CO product is observed, either coming from HCO decomposition, with an E<sub>a</sub> of 0.36 eV, or through the redox mechanism, with an E<sub>a</sub> of 0.47 eV. At this point, one may wonder why the RWGS reaction does not proceed through a redox route having an initial lower energy barrier than the HCOO route. A plausible response is found in the high hydrogen adatom, H\*, coverage of the Mo<sub>2</sub>C catalyst above 350 K. Given that the lateral interactions between H\* are negligible,<sup>27</sup> the formate associate pathway is favorable, and CO<sub>2</sub> dissociation is inhibited. Only when H\* decreases, the formation of CO\* species is possible through the redox path.

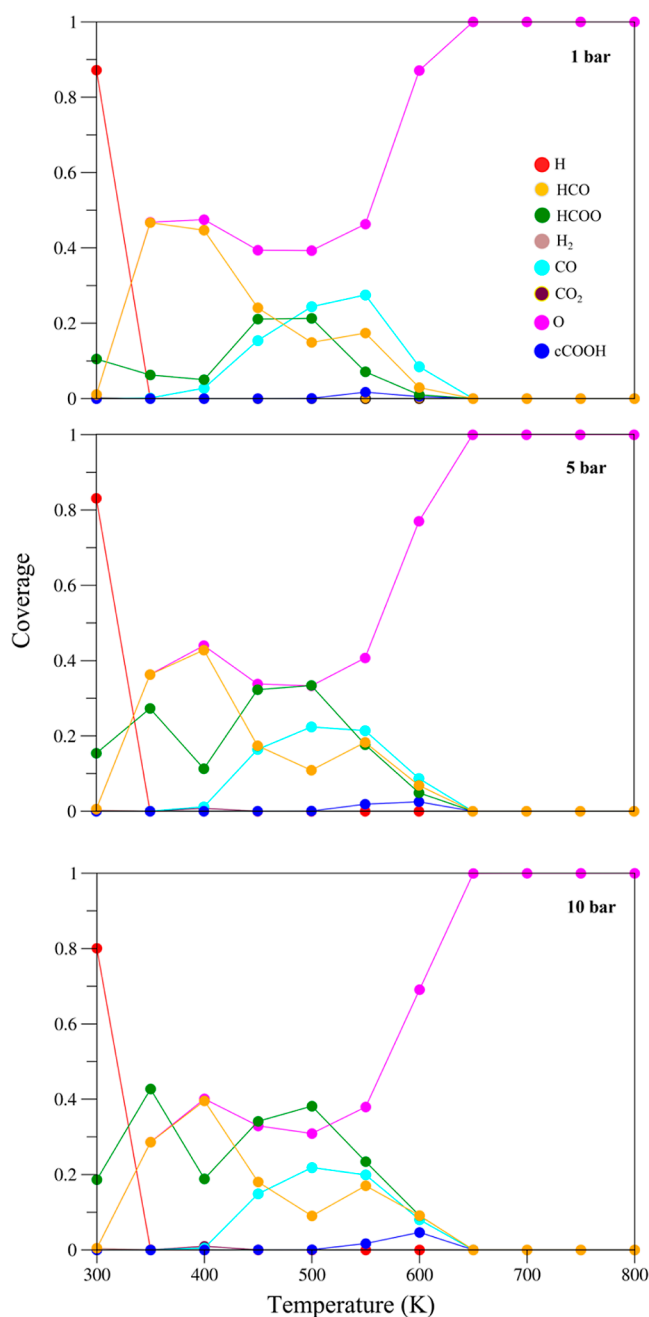


**Figure 5.** Variation of the surface coverage with the temperature for the RWGS reaction species on the  $\text{Mo}_2\text{C}$  MXene (0001) surface with input  $\text{H}_2/\text{CO}_2$  2:1 ratio and carried out at three different total pressures: 1, 5, and 10 bar, shown in top, middle, and bottom panels, respectively.

To measure the instantaneous efficiency of the  $\text{Mo}_2\text{C}$  MXene as a RWGS catalyst, we analyzed the turnover frequency (TOF), defined here as the number of molecules generated per site and second. This analysis allows us to identify the optimal pressure and temperature conditions at which the RWGS reaction has the largest production (or TOF number). Figure 6 depicts a heating contours map for the RWGS using three  $\text{H}_2/\text{CO}_2$  ratios of 2:1, 1:1, and 1:2 for the CO production. By using this type of maps, one can identify the effect of the partial pressure on the final production. The TOF scale depicted in Figure 6 corresponds to the CO production, generated in the 400–650 K temperature range,

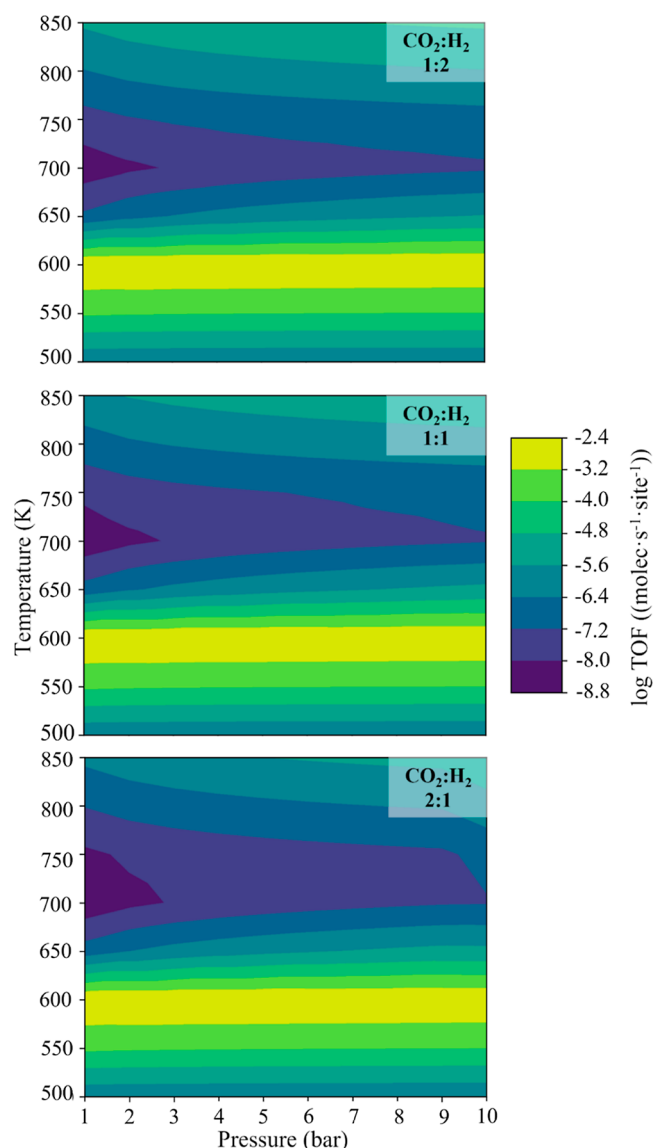


**Figure 6.** Heating map of TOF under different  $p$  and  $T$  working conditions for the RWGS reaction on the (0001)  $\text{Mo}_2\text{C}$  MXene surface for the CO production. Units for pressure, temperature, and TOF are bar, K, and  $\text{molecules}\cdot\text{site}^{-1}\cdot\text{s}^{-1}$ , respectively. The TOF scale corresponds to the common logarithm with base 10.

see Figure 5, with similar heating maps considering the TOF of water reported in Figure S3 in the Supporting Information. Even if CO is produced in the 400–650 K temperature range, reasonable TOF values for water require a higher temperature. This prediction is somehow expected given the aforementioned high energy barriers to form  $\text{OH}^*$  and  $\text{H}_2\text{O}^*$ , see Figure 4. In other words, the  $\text{Mo}_2\text{C}$  MXene surface easily dissociates  $\text{H}_2\text{O}$  into  $\text{HO} + \text{H}$ , as predicted in an earlier work,<sup>53</sup> and higher temperatures are needed to hydrogenate O adatoms toward water.<sup>22</sup>

Focusing on CO production, the present multiscale analysis predicts that the highest production will take place at  $\sim 600$  K, see Figure 6. Interestingly, such production is not affected neither by the  $\text{CO}_2/\text{H}_2$  ratio nor by the total pressure. To clarify the analysis, we focus on the  $\text{CO}_2/\text{H}_2$  1:2 ratio. Here, one can see that the temperature range of maximum  $\text{CO}^*$  production matches with the same range where the MXene surface is partially covered by CO species; see cyan dots in

Figure 5. On the other hand, the CO<sub>2</sub>/H<sub>2</sub> ratio only affects the region where the TOF has the lowest values; the blue dark regions of the Figure 6 heatmap. Furthermore, the present simulations indicate that the water production is significantly lower than that of CO and that the highest TOF values are reached at high temperatures, above 800 K, and using high pressures, around 10 bar, see Figure S3. Finally, we note that the water production is affected by the CO<sub>2</sub>/H<sub>2</sub> ratio, being more favorable with a H<sub>2</sub> partial pressure higher than that of CO<sub>2</sub>. The apparent activation route for each route can be estimated directly from our microkinetic simulations and values of 2.83, 2.70, and 2.22 eV are obtained for the redox, HCOO, and COOH routes at 700 K.

To summarize, the Mo<sub>2</sub>C MXene basal surface constitutes an appropriate heterogeneous catalyst candidate for the RWGS reaction. The formation of CO is easily achieved at low pressures and ~600 K (~300 °C), but water generation demands higher pressures and temperatures that can compromise the stability of the catalyst, but leave the path open to swing operando conditions where CO is first generated and released, and later, the O-terminated MXene is regenerated by hydrogenating O\* species to H<sub>2</sub>O at larger temperatures (~550 °C).<sup>26</sup> Attending to the stability of Ti<sub>3</sub>C<sub>2</sub>,<sup>29</sup> this temperature does not compromise, in principle, the stability of its Ti<sub>2</sub>C counterpart.

Available experimental data reported for MoC, Mo<sub>2</sub>C catalysts derived from these carbides show that these systems exhibit different performances for the RWGS reaction. For instance, Mo<sub>2</sub>C, MoC<sub>1-x</sub>, and Mo<sub>x</sub>C<sub>y</sub>/SiO<sub>2</sub> catalysts promote CO<sub>2</sub> conversion below 20 bar, 240 °C, and H<sub>2</sub>/CO<sub>2</sub> ratio equal to 16:3 conditions.<sup>54</sup> Other catalysts involving semi-conducting materials such as MoC/TiO<sub>2</sub> and MoC<sub>2</sub>/ZrO<sub>2</sub> transform CO<sub>2</sub> below 20 bar, 250 °C, and H<sub>2</sub>/CO<sub>2</sub> ratio equal to 5:1 conditions.<sup>55</sup> Finally, β-Mo<sub>2</sub>C, Cu/Mo<sub>2</sub>C, Cs/Mo<sub>2</sub>C, and Cu/Cs–Mo<sub>2</sub>C catalysts requires similar pressures 20 bar but lower temperature (150 °C) and H<sub>2</sub>/CO<sub>2</sub> ratio of 3:1.<sup>56</sup> By this comparison, one can conclude that the relative mild conditions at which CO is produced put the Mo<sub>2</sub>C MXene in a privileged position for using it as co-catalyst, either for the RWGS, or for subsequent hydrogenation processes aimed at obtaining new high-value chemicals such as CH<sub>4</sub> or CH<sub>3</sub>OH.

Before ending this section, we must highlight that there are two main differences between the Mo<sub>2</sub>C MXene and the pristine Mo<sub>2</sub>C surfaces making the first one a better candidate. The former has an intrinsic bidimensional nature that facilitates the interaction with the molecules and exposes the (0001) surface Mo-terminated. This latter surface is equivalent to the Mo<sub>2</sub>C(111) surface also terminated in Mo. This latter surface is difficult to realize experimentally, whereas the (0001) surface in MXenes is the exposed one. Additional information is provided in ref 28.

## 4. CONCLUSIONS

First-principles electronic structure calculations coupled to microkinetic simulations have been carried out to investigate the performance of the Mo<sub>2</sub>C MXene as a heterogenous catalyst for the RWGS reaction. This reaction requires relatively high temperatures to make the thermodynamics favorable. Indeed, temperatures around or higher than 700 K are found to be convenient for a reasonable production at a standard pressure of 1 bar. The three different RWGS mechanisms—redox, formate, and carboxyl routes—were investigated thoroughly by considering thermodynamic and

kinetics aspects. Among them, the redox and formate routes emerge as the most plausible for the Mo<sub>2</sub>C MXene-catalyzed RWGS reaction. The present analysis predicts that the formation of OH and the subsequent formation of H<sub>2</sub>O constitute the rate-limiting step to complete the reaction; meanwhile, CO formation is easily achieved.

Microkinetic simulations showed that, not surprisingly, the catalyst coverage can be altered by the total pressure, largely observed indeed for HCOO\* and HCO\* intermediates. On the other hand, the temperature range at which the CO is formed is found to be rather pressure-independent. By means of TOF heating maps as a function of *p*/*T* working conditions, we identified the optimal pressure and temperature situations at which the TOF acquires the maximum values. Our simulations conclude that the formation of CO is feasible at ~600 K and a low total pressure of 1 bar, and that such optimal conditions are maintained regardless the CO<sub>2</sub>/H<sub>2</sub> ratio. Although the formation of CO is relatively accessible, water formation requires harsher conditions, observable at ~800 K and above 5 bar, and it is also predicted that low CO<sub>2</sub>/H<sub>2</sub> ratios may promote the H<sub>2</sub>O formation at total pressure below 5 bar.

All in all, the present multiscale analysis poses Mo<sub>2</sub>C MXene as a catalyst candidate for the RWGS reaction, thus contributing to CO<sub>2</sub> valorization economy by converting this waste product into generating CO, a precursor toward the formation of CH<sub>4</sub> or CH<sub>3</sub>OH. Because the Mo<sub>2</sub>C MXene is able to produce CO through the RWGS reaction under mild conditions, one can also speculate about using it as a co-catalyst in subsequent CO hydrogenation processes leading to higher added value chemicals such as CH<sub>4</sub> or CH<sub>3</sub>OH.

## ■ ASSOCIATED CONTENT

### Supporting Information

The Supporting Information is available free of charge at <https://pubs.acs.org/doi/10.1021/acscatal.2c04489>.

Calculated frequencies, energy profile of the RWGS, transition state schemes, brief description of the microkinetic simulations, and heating maps of TOF versus *p*/*T* of RWGS for H<sub>2</sub>O production (PDF)

## ■ AUTHOR INFORMATION

### Corresponding Authors

Ángel Morales-García – *Departament de Ciència de Materials i Química Física & Institut de Química Teòrica i Computacional (IQTUCB), Universitat de Barcelona, 08028 Barcelona, Spain; [orcid.org/0000-0003-0491-1234](https://orcid.org/0000-0003-0491-1234); Email: [angel.morales@ub.edu](mailto:angel.morales@ub.edu)*

Francesc Illas – *Departament de Ciència de Materials i Química Física & Institut de Química Teòrica i Computacional (IQTUCB), Universitat de Barcelona, 08028 Barcelona, Spain; [orcid.org/0000-0003-2104-6123](https://orcid.org/0000-0003-2104-6123); Email: [francesc.illas@ub.edu](mailto:francesc.illas@ub.edu)*

### Authors

Anabel Jurado – *Departament de Ciència de Materials i Química Física & Institut de Química Teòrica i Computacional (IQTUCB), Universitat de Barcelona, 08028 Barcelona, Spain*

Francesc Viñes – *Departament de Ciència de Materials i Química Física & Institut de Química Teòrica i Computacional (IQTUCB), Universitat de Barcelona,*

08028 Barcelona, Spain; [orcid.org/0000-0001-9987-8654](https://orcid.org/0000-0001-9987-8654)

Complete contact information is available at:  
<https://pubs.acs.org/10.1021/acscatal.2c04489>

## Notes

The authors declare no competing financial interest.

## ACKNOWLEDGMENTS

This study has been supported by the Spanish Ministry of Science and Innovation (MICIN) through the project MCIN/AEI/10.13039/501100011033 PID2021-126076NB-I00, TED2021-129506B-C22, PID2020-115293RJ-I00, and the CEX2021-001202-M *María de Maeztu* unit of excellence. *Red Española de Supercomputación* (RES) is also acknowledged for the generous computational resources provides through the QHS-2021-3-0021 project.

## REFERENCES

- (1) Catlow, C. R.; Davidson, M.; Hardacre, C.; Hutchings, G. J. Catalysis Making The World a Better Place. *Philos. Trans. R. Soc., A* **2016**, *374*, 20150089.
- (2) Friend, C. M.; Xu, B. Heterogeneous Catalysis: A Central Science for a Sustainable Future. *Acc. Chem. Res.* **2017**, *50*, 517–521.
- (3) Whang, H. S.; Lim, J.; Choi, M. S.; Lee, J.; Lee, H. Heterogeneous catalysts for catalytic CO<sub>2</sub> conversion into value-added chemicals. *BMC Chem. Eng.* **2019**, *1*, 9.
- (4) Morales-García, Á.; Viñes, F.; Gomes, J. R. B.; Illas, F. Concepts, Models, and Methods in Computational Heterogeneous Catalysis Illustrated through CO<sub>2</sub> Conversion. *Wiley Interdiscip. Rev.: Comput. Mol. Sci.* **2021**, *11*, No. e1530.
- (5) He, Y. L.; Yang, K. R.; Yu, Z. W.; Fishman, Z. S.; Achola, L. A.; Tobin, Z. M.; Heinlein, J. A.; Hu, S.; Suib, S. L.; Batista, V. S.; Pfefferle, L. D. Catalytic manganese oxide nanostructures for the reverse water gas shift reaction. *Nanoscale* **2019**, *11*, 16677–16688.
- (6) Saeidi, S.; Najari, S.; Fazlollahi, F.; Nikoo, M. F.; Sefidkon, F.; Klemeš, J. J.; Baxter, L. L. Mechanisms and kinetics of CO<sub>2</sub> hydrogenation to value-added products: A detailed review on current status and future trends. *Renewable Sustainable Energy Rev.* **2017**, *80*, 1292–1311.
- (7) Su, X.; Yang, X. L.; Zhao, B.; Huang, Y. Q. Designing of highly selective and high-temperature durable RWGS heterogeneous catalysts: recent advances and the future directions. *J. Energy Chem.* **2017**, *26*, 854–867.
- (8) Ginés, M. J. L.; Marchi, A. J.; Apesteguía, C. R. Kinetic study of the reverse water-gas shift reaction over CuO/ZnO/Al<sub>2</sub>O<sub>3</sub> catalysts. *Appl. Catal., A* **1997**, *154*, 155–171.
- (9) Daza, Y. A.; Kent, R. A.; Yung, M. M.; Kuhn, J. N. Carbon Dioxide Conversion by Reverse Water-Gas Shift Chemical Looping on Perovskite-type Oxides. *Int. Eng. Chem. Res.* **2014**, *53*, 5828–5837.
- (10) Dong, Q.; Yin, S.; Guo, C. S.; Sato, T. Ce<sub>0.5</sub>Zr<sub>0.4</sub>Sn<sub>0.1</sub>O<sub>2</sub>/Al<sub>2</sub>O<sub>3</sub> catalysts with enhanced oxygen storage capacity and high CO oxidation activity. *Catal. Sci. Technol.* **2012**, *2*, 2521–2524.
- (11) Graciani, J.; Mudiyansele, K.; Xu, F.; Baber, A. E.; Evans, J.; Senanayake, S. D.; Stacchiola, D. J.; Liu, P.; Hrbek, J.; Sanz, J. F.; Rodriguez, J. A. Highly active copper-ceria and copper-ceria-titania catalysts for methanol synthesis from CO<sub>2</sub>. *Science* **2014**, *345*, 546–550.
- (12) Álvarez Galván, C.; Schumann, J.; Behrens, M.; Fieero, J. L. G.; Schlogl, R.; Frei, E. Reverse Water-gas Shift Reaction at the Cu/ZnO Interface: Influence of the Cu/Zn ratio on Structure-Activity Correlations. *Appl. Catal., B* **2016**, *195*, 104–111.
- (13) Ishito, N.; Hara, K. J.; Nakajima, K.; Fukuoka, A. Selective Synthesis of Carbon Monoxide via Formates in Reverse Water-Gas Shift Reaction Over Alumina-Supported Gold Catalyst. *J. Energy Chem.* **2016**, *25*, 306–310.
- (14) Ramanathan, S.; Oyama, S. T. New Catalysts for Hydro-processing: Transition Metal Carbides and Nitrides. *J. Phys. Chem.* **1995**, *99*, 16365–16372.
- (15) Chen, J. G. Carbide and Nitride Overlayers on Early Transition Metal Surfaces: Preparation, Characterization, and Reactivities. *Chem. Rev.* **1996**, *96*, 1477–1498.
- (16) Porosoff, M. D.; Yang, X.; Boscoboinik, J. A.; Chen, J. G. Molybdenum Carbide as Alternative Catalysts to Precious Metals for Highly Selective Reduction of CO<sub>2</sub> to CO. *Angew. Chem., Int. Ed.* **2014**, *53*, 6705–6709.
- (17) Ma, Y.; Guo, Z.; Jiang, Q.; Wu, K.-H.; Gong, H.; Liu, Y. Molybdenum carbide clusters for thermal conversion of CO<sub>2</sub> to CO via reverse water-gas shift reaction. *J. Energy Chem.* **2020**, *50*, 37–43.
- (18) Posada-Pérez, S.; Viñes, F.; Rodriguez, J. A.; Illas, F. Fundamentals of Methanol Synthesis on Metal Carbide Based Catalysts: Activation of CO<sub>2</sub> and H<sub>2</sub>. *Top. Catal.* **2015**, *58*, 159–173.
- (19) Naguib, M.; Kurtoglu, M.; Presser, V.; Lu, J.; Niu, J.; Heon, M.; Hultman, L.; Gogotsi, Y.; Barsoum, M. W. Two-Dimensional Nanocrystals Produced by Exfoliation of Ti<sub>3</sub>AlC<sub>2</sub>. *Adv. Mater.* **2011**, *23*, 4248–4253.
- (20) Naguib, M.; Barsoum, M. W.; Gogotsi, Y. Ten Years of Progress in the Synthesis and Development of MXenes. *Adv. Mater.* **2021**, *33*, 2103393.
- (21) Alhabeb, M.; Maleski, K.; Anasori, B.; Lelyukh, P.; Clark, L.; Sin, S.; Gogotsi, Y. Guidelines for Synthesis and Processing of Two-Dimensional Titanium Carbide (Ti<sub>3</sub>C<sub>2</sub>T<sub>x</sub> MXene). *Chem. Mater.* **2017**, *29*, 7633–7644.
- (22) Persson, I.; Halim, J.; Lind, H.; Hansen, T. W.; Wagner, J. B.; Näslund, L.; Darakchieva, V.; Palisaitis, J.; Rosen, J.; Persson, P. O. Å. 2D Transition Metal Carbides (MXenes) for Carbon Capture. *Adv. Mater.* **2018**, *31*, 1805472.
- (23) Kamysbayev, V.; Filatov, A. S.; Hu, H.; Rui, X.; Lagunas, F.; Wang, D.; Klie, R. F.; Talapin, D. V. Covalent Surface Modifications and Superconductivity of Two-Dimensional Metal Carbide MXenes. *Science* **2020**, *369*, 979–983.
- (24) Morales-García, Á.; Fernández-Fernández, A.; Viñes, F.; Illas, F. CO<sub>2</sub> Abatement Using Two-Dimensional MXenes Carbides. *J. Mater. Chem. A* **2018**, *6*, 3381–3385.
- (25) Morales-Salvador, R.; Morales-García, Á.; Viñes, F.; Illas, F. Two-dimensional nitrides as highly efficient potential candidates for CO<sub>2</sub> capture and activation. *Phys. Chem. Chem. Phys.* **2018**, *20*, 17117–17124.
- (26) Morales-Salvador, R.; Gouveia, J. D.; Morales-García, Á.; Viñes, F.; Gomes, J. R. B.; Illas, F. Carbon Capture and Usage by MXenes. *ACS Catal.* **2021**, *11*, 11248–11255.
- (27) López, M.; Morales-García, Á.; Viñes, F.; Illas, F. Thermodynamics and Kinetics of Molecular Hydrogen Adsorption and Dissociation on MXenes: Relevance to Heterogeneously Catalyzed Hydrogenation Reactions. *ACS Catal.* **2021**, *11*, 12850–12857.
- (28) Morales-García, Á.; Calle-Vallejo, F.; Illas, F. MXenes: New Horizons in Catalysis. *ACS Catal.* **2020**, *10*, 13487–13503.
- (29) Li, Z.; Wang, L.; Sun, D.; Zhang, Y.; Liu, B.; Hu, Q.; Zhou, A. Synthesis and thermal stability of two-dimensional carbide MXene Ti<sub>3</sub>C<sub>2</sub>. *Mater. Sci. Eng., B* **2015**, *191*, 33–40.
- (30) Jurado, A.; Morales-García, Á.; Viñes, F.; Illas, F. Identifying the Atomic Layer Stacking of Mo<sub>2</sub>C MXene by Probe Molecule Adsorption. *J. Phys. Chem. C* **2021**, *125*, 26808–26813.
- (31) Posada-Pérez, S.; RamírezGutiérrez, P. R.; Stacchiola, D.; Viñes, F.; Liu, P.; Illas, F.; Rodriguez, J. A. The Conversion of CO<sub>2</sub> to Methanol on orthorhombic β-Mo<sub>2</sub>C and Cu/β-Mo<sub>2</sub>C Catalysts: Mechanism for Admetol Induced Change in the Selectivity and Activity. *Catal. Sci. Technol.* **2016**, *6*, 6766–6777.
- (32) Kresse, G.; Furthmüller, J. Efficient iterative schemes for ab initio total-energy calculations using a plane-wave basis set. *Phys. Rev. B: Condens. Matter Mater. Phys.* **1996**, *54*, 11169.
- (33) Perdew, J. P.; Burke, K.; Ernzerhof, M. Generalized Gradient Approximation Made Simple. *Phys. Rev. Lett.* **1996**, *77*, 3865–3868.
- (34) Grimme, S.; Antony, J.; Ehrlich, S.; Krieg, S. A consistent and accurate ab initio parametrization of density functional dispersion

correction (DFT-D) for the 94 elements H-Pu. *J. Chem. Phys.* **2010**, *132*, 154104.

(35) Blöchl, P. E. Projector Augmented-Wave Method. *Phys. Rev. B: Condens. Matter Mater. Phys.* **1994**, *50*, 17953.

(36) Henkelman, G.; Uberuaga, B. P.; Jónsson, H. A. A climbing image nudged elastic band method for finding saddle points and minimum energy paths. *J. Chem. Phys.* **2000**, *113*, 9901.

(37) Henkelman, G.; Jónsson, H. A. A dimer method for finding saddle points on high dimensional potential surfaces using only first derivatives. *J. Chem. Phys.* **1999**, *111*, 7010.

(38) Rogal, J.; Reuter, K. Ab Initio Atomistic Thermodynamic for Surfaces: A Primer. *Experiment, Modeling and Simulation of Gas Surface Interactions for Reactive Flows in Hypersonic Flights*; Educational Notes RTO-EN-AVT-142: Neuilly-sur-Seine, France, 2007; Vol. 2, pp 1–18.

(39) Filot, I. A. W. *Introduction to Microkinetic Modeling*; Technische Universiteit Eindhoven: Eindhoven, 2018; p 217.

(40) Laidler, K. J.; King, M. C. The Development of Transition-State Theory. *J. Phys. Chem.* **1983**, *87*, 2657–2664.

(41) Truhlar, D. G.; Garrett, B. C.; Klippenstein, S. J. Current Status of Transition-State Theory. *J. Phys. Chem.* **1996**, *100*, 12771–12800.

(42) Pogodin, S.; López, N. A More Accurate Kinetic Monte Carlo Approach to a Monodimensional Surface Reaction: The Interaction of Oxygen with the RuO<sub>2</sub>(110) Surface. *ACS Catal.* **2014**, *4*, 2328–2332.

(43) Liu, J.; Xu, M.; Nordmeyer, T.; Zaera, F. Sticking Probabilities for CO Adsorption on Pt(111) Surfaces Revisited. *J. Phys. Chem.* **1995**, *99*, 6167–6175.

(44) Hellsing, B.; Kasemo, B.; Ljungström, S.; Rosén, A.; Wahnström, T. Kinetic model and experimental results for H<sub>2</sub>O and OH production rates on Pt. *Surf. Sci.* **1987**, *189–190*, 851–860.

(45) McCabe, R. W.; Schmidt, L. D. binding states of CO and H<sub>2</sub> on clean and oxidized (111)Pt. *Surf. Sci.* **1977**, *65*, 189–209.

(46) Manadé, M.; Viñes, F.; Gil, A.; Illas, F. On the H<sub>2</sub> Interactions with Transition Metal Adatoms Supported on Graphene: A Systematic Density Functional Theory. *Phys. Chem. Chem. Phys.* **2018**, *20*, 3819–3830.

(47) King, A. D.; King, R. B.; Yang, D. B. Homogeneous Catalysis of the Water Gas Shift Reaction Using Iron Pentacarbonyl. *J. Am. Chem. Soc.* **1980**, *102*, 1028–1032.

(48) Granda-Marulanda, L. P.; Rendón-Calle, A.; Builes, S.; Illas, F.; Koper, M. T. M.; Calle-Vallejo, F. A Semiempirical Method to Detect and Correct DFT-Based Gas-Phase Errors and Its Application in Electrocatalysis. *ACS Catal.* **2020**, *10*, 6900–6907.

(49) Jing, H.; Li, Q.; Wang, J.; Liu, D.; Wu, K. Theoretical Study of the Reverse Water Gas Shift Reaction on Copper Modified  $\beta$ -Mo<sub>2</sub>C(001) Surfaces. *J. Phys. Chem. C* **2019**, *123*, 1235–1251.

(50) Tibiletti, D.; Goguet, A.; Meunier, F. C.; Breen, J. P.; Burch, R. On the Importance of Steady-State Isotropic Techniques for the Investigation of the Mechanism of the Reverse Water-Gas-Shift Reaction. *Chem. Commun.* **2004**, 1636–1637.

(51) Cadi-Essadek, A.; Roldan, A.; Aparicio-Anglès, X.; de Leeuw, N. H. CO<sub>2</sub> and H<sub>2</sub> Adsorption and Reaction at Ni<sub>9</sub>/YSZ(111) Interfaces: A Density Functional Theory Study. *J. Phys. Chem. C* **2018**, *122*, 19463–19472.

(52) Zhang, X.; Zhu, X. B.; Lin, L. L.; Yao, S. Y.; Zhang, M. T.; Liu, X.; Wang, X.; Li, Y.-W.; Shi, C.; Ma, D. Highly Dispersed Copper over  $\beta$ -Mo<sub>2</sub>C as an Efficient and Stable Catalyst for the Reverse Water Gas Shift (RWGS) Reaction. *ACS Catal.* **2017**, *7*, 912–918.

(53) Gouveia, J. D.; Morales-García, Á.; Viñes, F.; Illas, F.; Gomes, J. R. B. MXenes as promising catalysts for water dissociation. *Appl. Catal., B* **2020**, *260*, 118191.

(54) Blanco, A. A. G.; Furlong, O. J.; Stacchiola, D. J.; Sapag, K.; Nazzarro, M. S. Porous Mo<sub>x</sub>C<sub>y</sub>/SiO<sub>2</sub> Material for CO<sub>2</sub> Hydrogenation. *Top. Catal.* **2019**, *62*, 1026–1034.

(55) Hamdan, M. A.; Nassereddine, A.; Checa, R.; Jahjah, M.; Pinel, C.; Piccolo, L.; Perret, N. Supported Molybdenum Carbide and Nitride Catalysts for Carbon Dioxide Hydrogenation. *Front. Chem.* **2020**, *8*, 452–464.

(56) Dongil, A. B.; Zhang, Q.; Pastor-Pérez, L.; Ramírez-Reina, T.; Guerrero-Ruiz, A.; Rodríguez-Ramos, I. Effect of Cu and Cs in the  $\beta$ -Mo<sub>2</sub>C System for CO<sub>2</sub> Hydrogenation to Methanol. *Catalysts* **2020**, *10*, 1213.